

Simultaneous Ultraviolet and X-ray Observations of the Seyfert Galaxy NGC 4151. I. Physical Conditions in the X-ray Absorbers

S. B. Kraemer^{1,2}, I.M. George^{3,4}, D.M. Crenshaw⁵, J.R. Gabel⁶, T.J. Turner^{3,4}, T.R. Gull², J.B. Hutchings⁷, G.A. Kriss⁸, R.F. Mushotzky⁴, H. Netzer⁹, B.M. Peterson¹⁰, & Ehud Behar¹¹

ABSTRACT

We present a detailed analysis of the intrinsic X-ray absorption in the Seyfert 1 galaxy NGC 4151 using *Chandra*/High Energy Transmission Grating Spectrometer data obtained 2002 May as part of a program which included simultaneous ultraviolet (UV) spectra using the *Hubble Space Telescope*/Space Telescope Imaging Spectrograph and the *Far Ultraviolet Spectrographic Explorer*. Previous studies, most recently using *ASCA* spectra, revealed a large ($> 10^{22}$ cm⁻²) column of intervening gas, which has varied both in ionization state and total column density. NGC 4151 was in a relatively low flux state during the observations reported here ($\sim 25\%$ of its historic maximum), although roughly 2.5 times as bright in the 2–10 keV band as during a *Chandra* observation in 2000. At both

¹Institute for Astrophysics and Computational Sciences, Department of Physics, The Catholic University of America, Washington, DC 20064; kraemer@yancey.gsfc.nasa.gov

²Exploration of the Universe Division, Code 667, NASA's Goddard Space Flight Center, Greenbelt, MD 20771

³Physics Department, University of Maryland, Baltimore County, Baltimore, MD 21250

⁴Exploration of the Universe Division, Code 662, NASA Goddard Space Flight Center, Greenbelt, MD 20771

⁵Department of Physics and Astronomy, Georgia State University, Atlanta, GA 30303

⁶University of Colorado, CASA, UCB 389, Boulder, CO 80309-0389

⁷Dominion Astrophysical Observatory, National Research Council of Canada, Victoria, BC V8X4M6, Canada

⁸Space Telescope Science Institute, 3800 San Martin Dr. Baltimore, Md 21218

⁹School of Physics and Astronomy, Raymond and Beverly Sackler Faculty of Exact Sciences, Tel-Aviv University, Tel-Aviv 69978, Israel

¹⁰Department of Astronomy, The Ohio State University, 140 W. 18th Ave., Columbus, OH 43210-106

¹¹Department of Physics, Technion, Haifa, 32000, Israel

epochs, the soft X-ray band was dominated by emission lines, which show no discernible variation in flux between the two observations. The 2002 *Chandra* data show the presence of a very highly ionized absorber, in the form of H-like and He-like Mg, Si, and S lines, as well as lower ionization gas via the presence of inner-shell absorption lines from lower-ionization species of these elements. The latter accounts for both the bulk of the soft X-ray absorption and the high covering factor UV absorption lines of O VI, C IV, and N V with outflow velocities $\approx 500 \text{ km s}^{-1}$. The presence of high ionization gas, which is not easily detected at low resolution (e.g., with *ASCA*), appears common among Seyfert galaxies. Since this gas is too highly ionized to be radiatively accelerated in sources such as NGC 4151, which is radiating at a small fraction of its Eddington Luminosity, it may be key to understanding the dynamics of mass outflow. We find that the deeper broad-band absorption detected in the 2000 *Chandra* data is the result of both 1) lower ionization of the intervening gas due to the lower ionizing flux and 2) a factor of ~ 3 higher column density of the lower ionization component. To account for this bulk motion, we estimate that this component must have a velocity $\gtrsim 1250 \text{ km s}^{-1}$ transverse to our line-of-sight. This is consistent with the rotational velocity of gas arising from the putative accretion disk. While both thermal wind and magneto-hydrodynamic models predict large non-radial motions, we suggest that the latter mechanism is more consistent with the results of the photoionization models of the absorbers

Subject headings: galaxies: individual (NGC 4151) — galaxies: Seyfert — X-ray: galaxies

1. Introduction

Mass outflow, revealed by intrinsic blue-shifted absorption lines in ultraviolet (UV) and X-ray spectra, appears to be ubiquitous among AGN (Crenshaw, Kraemer, & George 2003). For example, more than 50% of Seyfert galaxies observed with the spectrographs aboard the *Hubble Space Telescope (HST)* (Crenshaw et al. 1999) and with the *Far Ultraviolet Spectroscopic Explorer (FUSE)* (Kriss 2002) show UV absorption lines. While X-ray spectra obtained with *ASCA* showed absorption features such as bound-free edges of O VII and O VIII, in a similarly large fraction of Seyferts (Reynolds 1997; George et al. 1998), the blue-shifted absorption lines detected in high-resolution spectra from *Chandra* and *XMM-Newton* proved that the X-ray absorbing gas is also outflowing from the nuclei of these galaxies (e.g. Kaastra et al. 2000, 2002; Kaspri et al. 2000a; 2001; 2002). The high global

covering factors and kinetic luminosities inferred for the intrinsic absorbers suggests that they are a critical component of the central regions of AGN (Crenshaw et al. 2003, and references therein). However, many open questions remain, such as the physical connection, if any, between the UV and X-ray absorbers (e.g. Mathur et al. 1994; Kriss et al. 1995, 1996; Crenshaw & Kraemer 1999; Kraemer et al. 2002), the mechanism by which the outflowing gas is accelerated, e.g. thermal winds (Krolik & Begelman 1986), radiation pressure (Murray et al. 1995), or magnetically driven winds (Bottorff et al. 2000), and from whence the flows originate.

NGC 4151 ($cz = 995 \text{ km s}^{-1}$; determined from 21 cm observations: de Vaucouleurs et al. 1991), the nearest bright Seyfert 1 galaxy, has been extensively studied at all wavelengths. Ultraviolet observations, including those obtained with *IUE* (Boksenberg et al. 1978), the Hopkins Ultraviolet Telescope (Kriss et al. 1992), the *HST*/Goddard High Resolution Spectrograph (Weymann et al. 1997) and the *HST*/Space Telescope Imaging Spectrograph (STIS) (Crenshaw et al. 2000), revealed strong intrinsic absorption lines from species covering a wide range in ionization potential, as well as those from excited and metastable states of a number of ions. There is strong evidence that the ionization state of the UV absorbers is correlated with the flux of the continuum source (Bromage et al. 1985; Kraemer et al. 2001), as expected in photo-ionized gas. X-ray spectra show the effect of absorption by a large column of gas (Ives, Sanford, & Penston 1976), which is variable (e.g. Barr et al. 1977) and ionized (Yaqoob, Warwick, & Pounds 1989). Based on *ASCA* observations, George et al. (1998) were able to model the 0.6–10 keV X-ray continuum as a flat power law (photon index $\Gamma \sim 1.5$), modified by a photo-ionized absorber of column density $N_H \sim 10^{22-23} \text{ cm}^{-2}$. The gas was found to be in a fairly high ionization state, characterized by an ionization parameter, $U \sim 1$, where,

$$U = \frac{Q}{4\pi r^2 c n_H}, \quad (1)$$

and r is the radial distance of the absorber, n_H is the number density of hydrogen, and $Q = \int_{13.6\text{eV}}^{\infty} \frac{L_\nu}{h\nu} d\nu$, or the number of ionizing photons s^{-1} emitted by a source of luminosity L_ν ¹. Interestingly, the changes in the opacity of the X-ray absorber did not seem to depend on the flux state of the intrinsic continuum, and, in fact, there is some evidence that they are anti-correlated (see Weaver et al. 1994), which may be evidence for both a multi-component absorbing medium and bulk motion across our line-of-sight.

More recently, Schurch & Warwick (2002) used *BeppoSax* data from 1999 January and a

¹In George et al., the models were parameterized in terms of the “X-ray” ionization parameter, U_x , for which the integration is taken from 0.1 keV to 10 keV. They determined that $U_x = 0.06 - 0.08$; note that the conversion between U and U_x is sensitive to the shape of the ionizing continuum below 0.1 keV.

series of *ASCA* observations from 2000 May 15 – 20 to attempt to determine the nature of the X-ray absorber in NGC 4151. They were able to fit the data with a flat underlying power-law ($\Gamma \approx 1.65$), a contribution from a cold reflector, and a two-component absorber: an intrinsic neutral component with $N_H \approx 3.4 \times 10^{22} \text{ cm}^{-2}$ and a highly ionized absorber, with $N_H \approx 2.4 \times 10^{23} \text{ cm}^{-2}$ and an ionization parameter $U \sim 10$. However, Kraemer et al. (2001) analyzed UV spectra, obtained with STIS in 1999 July, and determined that the intrinsic column of low-ionization gas could not exceed a few $\times 10^{21} \text{ cm}^{-2}$, although it is possible that the amount of low-ionization gas was extremely variable over this period. The lack of contemporaneous high-resolution UV and X-ray spectra have hindered attempts to unravel the various components of intrinsic absorption in this object. To that end, we obtained near-simultaneous STIS, *FUSE*, and *Chandra*/High Energy Transmission Grating Spectrometer (HETGS) observations on 2002 May 9 –10. In this paper, we present our analysis of the X-ray continuum ($\sim 1\text{--}10 \text{ keV}$) and the imprinted absorption lines. The UV results will be presented in a subsequent paper (S.B. Kraemer et al., in preparation; hereafter Paper II), as will the results from a study of the soft X-ray emission lines and reflection component (I.M. George et al. in preparation, hereafter Paper III).

2. Observation and Data Reduction

The main data set considered in this paper was obtained during a *Chandra* observation of NGC 4151 over the period 2002 May 07 23:26 to May 11 14:14 (UTC). The observation was performed in two parts (*Chandra* ‘OBSIDs’ 3480 and 3052), with a gap of $\sim 17 \text{ hr}$ (May 09 01:34–18:26) during perigee and passage of the spacecraft through the Earth’s radiation belts. The HETGS (Marshall, Dewey & Ishibashi 2004) was deployed in the optical path, and the full ‘S-array’ of the Advanced CCD Imaging Spectrometer (ACIS; Garmire et al 2003) was used as the focal-plane detector (with an operating temperature of 153 K). To avoid the risk of telemetry saturation, only the central half of the ACIS-S array was read out, using a CCD frame-time of 1.8 s. The target was slightly offset from the nominal pointing direction (by 20 arcsec) to ensure the data within the zeroth-order image was always read-out using the same CCD node during the intentional dithering of the spacecraft.

In this paper we also refer to two other *Chandra* observations of NGC 4151. The first is that performed in 2000 March (OBSID 335) with a duration of $\sim 50 \text{ ks}$, and also using the HETGS/ACIS-S instrumental configuration. Some of the results of this observation have been presented previously by Ogle *et al.* (2000). The second additional *Chandra* observation referred to here was performed over the period 2002 July 02–03 (OBSID 3089). The ACIS-S array was also employed as the focal-plane detector for this observation, but with the Low-

Energy Transmission Grating Spectrometer (LETGS; Brinkman et al. 1997) deployed in place of the HETGS.

2.1. Data Reduction

The HETGS data from both epochs were processed using the `ciao` (v3.0.1) and `ftools` (v5.3.1) software packages, along with calibration files from the *Chandra* CALDB (v2.26) release². In the case of the observation using the LETGS, we used the more recent `ciao` (v3.2.0) and CALDB (v3.0.0) in order to incorporate the latest estimates of the spatial and temporal variations in this contamination³. We also made use of our own software for a number of the analysis tasks. The data were processed in the standard manner, including the removal of bad detector pixels and other detector artifacts, and removal of events with detector ‘grades’ *not* equal to 0, 2, 3, 4, or 6. The selection criteria used resulted in exposures of ~ 48 ks for the HETGS observation in 2000, ~ 93 and ~ 157 ks for the first and second segments of the HETGS observation in 2002 May, and ~ 84 ks for the LETGS observation in 2002 July.

The dispersed source spectra for the various grating arms were extracted using a strip centered on the corresponding dispersed spectrum, with a half-width (in the cross-dispersion direction) of 5×10^{-4} degrees. This corresponds to a distance of ~ 115 pc on the plane of the sky assuming a distance of 13.2 Mpc to NGC 4151. We are only concerned about the nucleus, although the extracted spectrum will include a contribution from the X-ray emission-line gas in the inner Narrow-Line Region (see Ogle et al. 2000).

The intrinsic energy resolution of the CCDs were used to distinguish between the overlapping orders in the dispersed spectra. The total number of counts in the source extraction cells with energies and positions consistent with the $\pm 1^{\text{st}}$ -order MEG spectra in the 0.5–7 keV band were 9436 for the observation in 2000, and 173186 for the combined HETGS observations in 2002 May. The corresponding number in the LEG during the observation in 2002 July was 97448 counts. From an analysis of strips adjacent and parallel to the source extraction cell, we estimate that in all cases $< 2\%$ of the counts in the extraction cell are due to background events (including the extended X-ray emission surrounding the nucleus). This background was therefore ignored during the analysis of the nuclear continuum presented

²Including the `acisD1999-08-13contamN0003.fits` file to correct for the time-dependent contamination on the surface of the CCDs (e.g. see Marshall et al. 2004).

³We have performed spot checks, and the use of the latest calibration files and software do not affect the conclusions presented here.

here.

The line-spread function of each of the gratings can be well-approximated by a Gaussian at all energies with a width $\sigma \simeq 2 \times 10^{-2}$, $\simeq 10^{-2}$, and $\simeq 5 \times 10^{-3}$ Å, for the 1st-order spectra of the LEG, MEG, and HEG (respectively). All the spectra were initially binned to this size, and the positive and negative orders were combined.

2.2. Temporal Analysis

The variability exhibited by the source during and between the two HETGS observations is illustrated in Fig. 1, which shows the coadded MEG and HEG 1st-order light curves in three energy bands. The data are shown using 1024 s bin, and for simplicity each light curve has been normalized to the error-weighted mean value of the (combined) 2002 observation. We find the count rate in the soft X-ray band (0.7–1.0 keV) during the 2002 observation to be consistent with a constant ($1.32 \pm 0.35 \times 10^{-2}$ count s⁻¹; $\chi^2 = 213$ for 219 degrees of freedom [dof]). The earlier 2000 observation has a consistent mean value ($1.52 \pm 0.42 \times 10^{-2}$ count s⁻¹) in this band, although with a hint of variability within the observation ($\chi^2 = 51$ for 41 dof). More interestingly, Fig. 1 clearly shows the source exhibited a dramatic change in intensity in both the medium and hard bands. In the medium (1.0-3.0 keV) band, NGC 4151 brightened by a factor of ~ 5 (to 0.52 ± 0.05 count s⁻¹) between 2000 and 2002, while in the hard (3.0-8.0 keV) band the increase was a factor ~ 3 (to 0.67 ± 0.05 count s⁻¹) between these epochs. The source does exhibit statistically-significant variations in intensity in both these bands during both epochs. However this is of relatively-low amplitude (maximum trough-to-peak amplitude of a factor ~ 1.9 in the medium band during the 2002 observations).

Light curves were also constructed in the above bands for the LETGS observation in 2002 July. The soft band light curve was found to be consistent with a constant ($2.21 \pm 0.04 \times 10^{-2}$ count s⁻¹; $\chi^2 = 64$ for 80 dof) during this epoch. As will be illustrated below, correcting for the differences in the spectral responses of the instruments, this LETGS count rate is consistent with the HETGS count rates quoted above in this band. The mean count rates in the medium and hard X-ray bands during the LETGS observations were 0.42 ± 0.04 count s⁻¹ and 0.64 ± 0.02 count s⁻¹ (respectively). As for the HETGS data, statistically-significant variations were evident in both bands during this epoch, again with maximum trough-to-peak amplitude of a factor ~ 1.9 . Thus hereafter we consider only the time-averaged spectra obtained during each epoch.

3. Spectral Analysis and Modeling

3.1. The Spectral Signature of the Intrinsic Absorber

Historically, the intrinsic X-ray continuum in NGC 4151 has been found to be heavily absorbed at energies $\lesssim 1$ keV (e.g., George et al. 1998, and references therein). To illustrate this, in Fig. 2 we show the time-averaged, broad-band spectra obtained during the three epochs. For clarity of display only the MEG data are shown for the HETGS observations, and in all cases the data have been rebinned such that each bin contains at least 30 photons. Each data set has been corrected for the appropriate instrumental response. As a result of the soft X-ray absorption, absorption lines from abundant elements such as C, N and O cannot be detected. In fact, the bound-free edges from O VII, O VIII, Ne IX, and Ne X, which were typically the signature of warm absorbers in the *ASCA* era (e.g. Reynolds 1997), are so deep that they are blended together and produce a smooth curvature at low resolution. In Fig 3 we show a direct comparison of the 2000 and 2002 HETGS spectra. In both epochs, the soft band is dominated by emission lines which have not varied significantly in flux, while the hard band is both weaker and more heavily absorbed in the earlier spectrum. During both observations, the intrinsic continuum below ~ 1 keV is so heavily absorbed that its contribution to the soft X-ray emission is negligible. However, with the 2002 spectra, we were able to detect absorption lines at energies > 1 keV from less abundant species, such as Mg, Si, and S. The ionic column densities measured from these lines, in combination with the broad-band spectral curvature, allows us to constrain the ionization state and column densities of the components of X-ray absorption.

As noted in Section 1, our analysis of the UV spectra will be presented separately. However the UV absorption provides crucial constraints for modeling the X-ray absorbers. To summarize the results of our UV analysis, we found that the bulk of the UV absorption is associated with component D+E, which has a velocity centroid of $v_r = -491 (\pm 8)$ km s^{-1} (Weymann et al. 1997; Kraemer et al. 2001). We were able to deconvolve D+E into three physically distinct components: a high covering factor component in which saturated OVI $\lambda\lambda$ 1031.9, 1037.6, N V $\lambda\lambda$ 1238.8, 1242.8, and C IV $\lambda\lambda$ 1548.2, 1550.8 lines arise (which we will refer to as D+Ea); a dense component responsible for the C III* λ 1175 absorption (D+Eb); and a component with a lower covering factor derived from the P V $\lambda\lambda$ 1117.8, 1128.1 lines (D+Ec). We also detected S IV λ 1062 absorption at $v_r \approx -215$ km s^{-1} , which suggests that the gas associated with UV component E' is more highly ionized than that modeled by Kraemer et al. (2001). Each of these components contributes to the X-ray absorption. The UV constraints for the X-ray modeling are listed in Table 1.

From the S, Si, and Mg absorption lines detected in the HETG spectrum, there is

strong evidence for highly ionized gas, in addition to the lower ionization gas that may be associated with the UV absorbers. This is clearly seen in the Si array (Fig. 4), which shows strong Si XIV λ 6.1804, 6.1858 and inner shell lines such as Si X $\lambda\lambda$ 6.854, 6.864 and those from lower states of ionization, but has relatively weak S XII $\lambda\lambda$ 6.717, 6.719 and Si XI λ 6.778. Although the Si XIII λ 6.648 line is affected by unocculted emission from the He-like triplet, its weakness relative to Si XIV is further evidence for absorbers of different ionization states, rather than a single, increasingly neutral column of gas. Therefore, we included a very highly ionized absorber to account for the H-like lines (X-High). Since the inner shell lines are from ionization states that can co-exist with the Li-like ions of C, N, and O, we assume that they arise in component D+E*a*. While there are no UV constraints on the covering factor (C_f) for X-High, the depths of the H-like lines suggest that C_f is fairly large, otherwise these lines would be significantly diluted (see Turner et al. 2005). Hence we assumed $C_f = 1.0$ for this component. While we were only able to constrain the radial velocities for the S XVI, Si XIV and Si XIII lines, we found v_r for the high ionization gas to be consistent with that of D+E (see Fig 5). The H-like lines appear to be narrow, although accurate measurements of their velocity dispersions are impossible due to partial filling by neighboring emission lines. Nevertheless, we assumed a dispersion $\sigma_v = 50 \text{ km s}^{-1}$ or roughly the thermal width for these ions in gas at a temperature of $\sim \text{few} \times 10^6 \text{ K}$, with the caveat that the intrinsic widths may indeed be substantially greater.

3.2. The Photoionization Models

The photoionization models for this study were generated using the Beta 5 version of Cloudy (G. Ferland 2003, private communication), which includes estimated $\Delta n=0$ dielectronic recombination (DR) rates for the M-shell states of Fe and the L-shell states of the third row elements (Kraemer, Ferland, & Gabel 2004). The absorbers were modeled as single-zoned slabs of constant-density atomic gas, irradiated by the central source. We assumed roughly solar elemental abundances (e.g. Grevesse & Anders 1989) and the absorbing gas was assumed to be free of cosmic dust. The logs of the elemental abundances, relative to H by number, are as follows: He: -1.00 , C: -3.47 , N: -3.92 , O: -3.17 , Ne: -3.96 , Na: -5.69 , Mg: -4.48 , Al: -5.53 , Si: -4.51 , P: -6.43 , S: -4.82 , Ar: -5.40 , Ca: -5.64 , Fe: -4.40 , and Ni: -5.75 . As per convention, the models are parameterized in terms of the ionization parameter U (see Section 1), and total hydrogen column density, N_H .

From our STIS spectrum, we measured an extinction-corrected UV flux at 1450\AA of $\sim 7.7 \times 10^{-26} \text{ ergs cm}^{-2} \text{ s}^{-1} \text{ Hz}^{-1}$ for an extinction $E_{B-V} = 0.04$ (Kriss et al. 1995). The 2–10 keV flux in the *Chandra* spectra was $\sim 1.9 \times 10^{-10} \text{ ergs cm}^2 \text{ s}^{-1}$. Due to the heavy

absorption, it is not possible to tightly constrain the intrinsic X-ray photon index. Although Zdziarski, Johnson & Magdziarz (1996), using combined *ROSAT*, *Ginga*, and *Gamma Ray Observatory*/OSSE data, derived a $\Gamma = 1.8$, Yaqoob & Warwick (1991) found that, like most Seyferts, NGC 4151 shows a anti-correlation between spectral slope and intensity. Therefore, we assumed $\Gamma = 1.5$, which is consistent with the 2002 data and previous low-flux state values. Based on this index, the unabsorbed flux is $\sim 2.7 \times 10^{-28}$ ergs cm^{-2} s^{-1} Hz^{-1} at 0.5 keV. Using these values, we modeled the spectral energy distribution (SED) as a broken power law of the form $L_\nu \propto \nu^\alpha$ as follows: $\alpha = -1.0$ for energies < 13.6 eV, $\alpha = -1.3$ over the range $13.6 \text{ eV} \leq h\nu < 0.5 \text{ keV}$, and $\alpha = -0.5$ above 0.5 keV. We included a low energy cut-off at 1.24×10^{-3} eV (1 mm) and a high energy cutoff at 100 keV. The model SED is similar to that used in Kraemer et al. (2001). The luminosity in ionizing photons is $Q = 1.1 \times 10^{53}$ photons s^{-1} . Note that, while the soft X-ray break could occur at lower energy, we found that a higher energy break causes an overprediction of the soft-X-ray continuum.

As described in the previous section, there is evidence for five distinct components with non-negligible X-ray opacities. Given the large covering factors of components D+Ea, D+Eb and E', the most straightforward geometry places the absorbers over a range in radial distances, with the more distant ones illuminated by an ionizing continuum that has been filtered by the intervening absorbers (a similar model was used for NGC 3516; Kraemer et al. [2002]). The only way to constrain the radial distance of a component is by determining both n_H and U , which we were only able to do for components D+Eb and E' (as we will show in Paper II). However, it is plausible that the X-High and D+Ea lie closest to the central source, since they are the most highly ionized. Also, in our previous study of NGC 4151 (Kraemer et al. 2001), we only found evidence for a small column ($\sim 10^{20} \text{ cm}^{-2}$) of high ionization gas in the shadow of component D+E. Therefore, we assumed that the absorbers were ordered in increasing radial distance as follows: X-High, D+Ea, D+Eb, and E'. Since D+Ec has a lower C_f , we assumed that it was co-located with D+Eb, i.e., only screened by the two higher ionization components, but did not include its affect on the filtered continuum used to model E'.

We generated a grid of photoionization models for a range of U and N_H values, beginning with X-High and following with associated grids for the screened components, using the transmitted continuum of each intervening component as the incident continuum for the next in radial order. The tables of ionic column densities predicted by Cloudy were used to construct a grid of high-resolution spectra, including the effects of bound-free absorption (Verner et al. 1996), and resonance and inner shell absorption lines (e.g., Behar & Netzer 2002). The spectral grids were used as an input to `xspec` in order to fit the broad-band X-ray spectrum. Our initial set of models, based on the constraints listed in Table 1, slightly underpredicted the X-ray absorption at energies $\lesssim 0.7$ keV. Since the soft X-ray emission in

these spectra are dominated by the emission-line gas, only a small fraction of the emission at these energies can be from the transmitted continuum (see Fig 3). Since the UV and X-ray continuum regions in NGC 4151 are suspected to have different sizes (Crenshaw et al. 1996; Edelson et al. 1996), using the UV lines may lead us to underestimate C_f for the X-ray source. Therefore, we allowed the covering factor (Table 1) to be $\sim 20\%$ higher, which improved the fit without the overprediction of the UV ionic column densities that would have occurred if the higher soft-X-ray opacity were the result of additional low-ionization gas.

The presence of a strong, narrow Fe $K\alpha$ (6.4 keV) and, perhaps, several other emission lines in the spectrum (e.g., see Figs. 2, 3) is indicative of fluorescence within optically-thick material within the circumnuclear regions following illumination by the primary X-ray continuum. Thus we have also included such a ‘reflection component’ (e.g. George & Fabian 1991; Matt et al. 1991) with our modeling. Unfortunately the location, geometry and ionization-state of such circumnuclear material is not very well constrained by current data (for any object). Thus neither are the precise details of the reflected spectrum (which included both fluorescent lines and a scattered continuum). However, besides offering an explanation for the Fe $K\alpha$ emission, the only significant effect of such a component for the results reported here is a slight flattening of the observed continuum at high energies ($\gtrsim 3$ keV). Thus we have simply assumed a ‘standard’ reflection component where the intensity of the reflected continuum is linked to the observed strength of the Fe $K\alpha$ line (using the calculations of George & Fabian 1991). Along with an incident primary continuum of $\Gamma = 1.5$, we assumed that the material subtends 2π sterad as seen from the central source, that the material has cosmic abundances, and is far from the central source and hence is effectively neutral. Our model also includes fluorescent lines from other abundant elements from the calculations of Matt, Fabian & Reynolds (1997).

3.3. Model Results

With the intrinsic continuum and reflection components held fixed, we generated a set of absorber models to fit the broad-band spectral properties. We deemed the modeling to be successful if the combined effects of the absorption and reflection provide a satisfactory fit to the spectrum at energies where the emission is dominated by the transmitted continuum, i.e. $\gtrsim 1.5$ keV, and the UV-derived constraints are met. The parameters of our best fitting models are listed in Table 2 and the predictions of ionic column densities are listed in Table 3. In Table 1, we compare the predicted ionic column densities to the UV constraints. The model is shown versus the combined MEG and HEG spectra in Fig. 6, while the opacities

of the individual components are shown in Fig. 7. The curvature seen above ~ 1 keV is primarily due to the bound-free edges from O VI (inner shell), O VII, and O VIII edges predicted by the component D+Ea and the Ne X and Fe XVII–XX edges from X-High. Note that a different set of solutions would be obtained if the radial locations of X-High and D+Ea were switched, due to the effect of the deep soft-X-ray absorption from D+Ea. Although we cannot rule out this scenario, we found that reversing the order of the models provides a less satisfactory fit to the curvature below ~ 2 keV, due to the overprediction of the O VIII column density in the high ionization component which results when the H- and He-like Mg, Si, and S columns are held fixed. Fig 8 shows the data/model ratio in the 2–5 keV band, where we have the best constraints on the transmitted continuum. After grouping the data such that there are at least 50 photons in each bin, a simultaneous comparison between the MEG and HEG data and our model in the 2–5 keV band gives a χ^2 -statistic of 1694 for 1708 degrees of freedom (i.e. a reduced χ^2 value of 0.992). Component D+Ea also produces the bulk of the absorption below 1 keV, although there is some contribution from the lower ionization intrinsic absorption, mostly due to He II bound-free absorption, and the Galactic neutral column ($N_H = 2.0 \times 10^{20} \text{ cm}^{-2}$; Murphy et al. 1996). Note that the model is not tightly constrained by the fit at energies < 1 keV, since the soft-X-ray emission is dominated by the extended emission-line gas, except in the sense that the transmitted continuum must be weaker than the observed X-ray emission over the entire soft band.

Next, we examined the predicted X-ray absorption line spectrum. Since the ionic column densities (N_{ion}) were determined by matching the broad-band spectral features, the absorption-line fit provides a consistency check for the models. We generated the line profiles based upon the N_{ion} 's, using the σ_v 's assumed for each component. As noted above, since the strong resonance lines of H- and He-like C, N, O, and Ne have energies < 1.2 keV, their imprint against the transmitted continuum is swamped by the extended soft emission, and our study is limited to the H-, He-like and inner shell lines of Mg, Si, and S. In Figs. 9, 10, and 11, we show portions of the time-averaged spectrum obtained by the HETGS in 2002. These regions were selected so as to contain all the $1s \rightarrow 2p$ transitions for H- through F-like ions of Mg, Si and S. The combined MEG and HEG 1st-order data are shown (after correction for the appropriate instrumental responses) and are displayed using 0.01Å bins (approximately the “ 1σ ” width of the spectral resolution of the MEG). The model predictions are overlaid on the data (the emission features are from the reflection component model and the spectra are consistent with K-shell features from the disk). The Mg lines, with energies < 1.5 keV, are in a region of the X-ray spectrum where the transmitted/absorbed continuum begins to become weak relative to the extended emission (see Fig 6). Therefore, it is difficult to determine the actual depths of most of the absorption lines and, our model appears to overpredict several of them. However, the fit is good for Mg VI (combined with

Fe XIX and Ne X) and Mg VII, and the features from the other Mg ions appear to be present, although shallower than the model predictions. For the S and Si arrays, where the transmitted/absorbed continuum dominates, the model provides a better overall fit to the absorption lines. In both cases, the model, primarily X-High, predicts the strong H-like and weaker He-like lines observed. The predictions for the inner shell lines are best assessed with the Si array (Fig. 10). Generally, the model (D+Ea) provides a fairly good fit, in the sense that all of the predicted lines are present in the spectrum. Nevertheless, Si IX and Si X are somewhat overpredicted and Si VI is underpredicted. We tested whether increasing N_H or decreasing U for D+Ea would drive Si to sufficiently lower ionization, but in doing so we overpredicted N_{PV} from this component. We also tested the effect varying σ_v . While the overpredictions are mitigated by assuming $\sigma_v = 85 \text{ km s}^{-1}$, the fit becomes worse for the underpredicted lines, and the opposite occurs for $\sigma_v = 285 \text{ km s}^{-1}$. However, the discrepancy corresponds to over/under-predictions of the ionic column densities by factor of < 2 . These could easily be the result of inaccuracies in the DR rates used in Cloudy, since the analytic form used for the third row elements does not include structure within the L-shell (see Gu 2003).

3.4. Comparison with 2000 HETGS Spectrum

One of the central questions in understanding the nature of intrinsic absorption and mass outflow in AGN is whether temporal variations in the spectral signature of the absorbers, including the appearance/disappearance of individual components, result from changes in ionization state or bulk motion (see Crenshaw et al. 2003). The 2002 LETGS spectrum found the X-ray continuum to be roughly the same flux and possess similar spectral characteristics as the 2002 HETGS observations (Fig 2). This suggests that the physical conditions in the X-ray absorber did not change between these observations; indeed, our model provides a reasonable fit to the LETGS data. The 2000 HETGS observations found NGC 4151 in a lower flux state than in 2002 (see Fig 3), with a steeper curvature above $\sim 1 \text{ keV}$, consistent with an increase in the opacity of the absorber, as expected if the gas had become more neutral in response to the drop in ionizing radiation. Noting that some of the drop in the X-ray flux must be due to the increased absorption, we estimate that the intrinsic flux was a factor of ~ 2 lower during the 2000 observation. Starting with X-High, we regenerated our set of models for this lower flux state, using the same SED and holding N_H fixed, and compared the results to the 2000 HETG spectrum. The model was unsuccessful in matching both the strength of the absorption and the curvature in the 2–5 keV range. We found little improvement when we decreased U for X-High by a factor of 3, which exceeds the maximum allowed by the data.

The mismatch between the models and the 2000 spectrum indicates that difference in the X-ray absorption cannot result simply from changes in ionization state. Instead, the total column density of the absorbers must have been greater in 2000, as suggested by Schurch & Warwick (2002) based on their analysis of the 2000 May *ASCA* observations. To test this, we let column density for D+Ea be a free parameter and obtained a rough fit to the 2–5 keV curvature for $\log N_H = 22.93$. The opacities of the low-state versions of X-High and D+Ea are shown in Fig 7. Under these conditions, the other screened components become effectively neutral, therefore we replaced them with a neutral column of $\log N_H = 21.7$. The model is shown against the data in Fig 12, and it provides a reasonable fit to the broadband spectrum, albeit with the assumption that the transmitted continuum has a negligible contribution to the observed flux below $\lesssim 2$ keV. We suggest that this is evidence for a combination of the response to the drop in ionizing flux and bulk motion across our line of sight. We will pursue this in Paper II via a detailed comparison of the 1999 and 2002 STIS spectra.

3.5. Physical Conditions within the Absorbers

Since the earliest UV (Boksenberg et al. 1978) and X-ray (Ives et al. 1976) observations, NGC 4151 has shown strong intrinsic absorption, which suggests that either 1) the absorbers are stable over relatively long periods ($\gtrsim 30$ yrs) or that 2) the gas is constantly replenished. The thermal stability of photoionized gas is illustrated via a thermal stability curve (“S-Curve”), which is a plot of the electron temperature, T_e , versus the “pressure” ionization parameter, U/T_e . There are two regimes of ionization for which photoionized gas is stable to thermal perturbations (see Krolik, McKee & Tarter 1981; Krolik & Kriss 2001): low ionization/temperature, when line cooling is efficient, and at high ionization/temperature, when Compton processes dominate. The intermediate region can be quasi-stable (when T_e versus U/T_e has a positive slope) or unstable (negative slopes) to thermal perturbations. Note that the form of the S-Curve is sensitive to the SED and the elemental abundances. Furthermore, if adiabatic cooling is included the maximum temperature can be considerably lower than the Compton temperature (see Chelouche & Netzer 2005). In Fig 13 we show the thermal stability curve derived for our model SED and abundances and indicate the positions of the 5 component models. For the most part, these components are not clustered near a single value of U/T_e , hence they are not in close pressure equilibrium with one another, with the exception of D+Ec and X-High, which may be coincidental given the fact that we assumed a filtered continuum for the former.

Not unexpectedly, the four UV components lie on the line-cooled part of the curve, since

the very fact that we detect absorption from Li-like CNO ions and lower ionization states requires there to be a non-negligible fraction of bound electrons. Note that these components, in particular E' , lie off the curve due to the fact that the models were generated with a filtered ionizing continuum (hence a different SED). The most highly ionized of these, $D+Ea$ lies near the transition between stable and quasi-stable sections of the curve. To examine its stability during high-flux states, we generated a model for an ionizing flux 4 times that observed in 2002, similar to historic high-states (see Kraemer et al. 2001). Although the high-state $D+Ea$ lies in the quasi-stable part of the curve, it would not be thermally unstable. Therefore, if this component has remained in our line-of-sight to the nucleus of NGC 4151, it would have always been seen in absorption, with a spectral signature that reflects changes in its ionization state in response to variations in the ionizing flux.

In the current epoch, X-High resides in a quasi-stable region below the Compton-cooled regime. For the high-state model, X-High is driven towards the Compton-cooled region, but remains in a quasi-stable state. We also examined the behavior of this component for a flux state 2 times lower than the present epoch, similar to the 2000 HETGS observations. Notably, X-High becomes thermally unstable as the flux drops. This suggests a possible scenario for the evolution of the absorbers. If the bulk of the absorbing gas originates in a highly ionized phase, similar to X-High, the gas could become thermally unstable during low-flux states. At these times, the gas may rapidly cool and recombine, until its physical state resembles that of $D+Ea$. If it has cooled/recombined sufficiently, it may remain thermally stable. This is what might be expected if the flow originates as a hot thermal wind (Krolik & Kriss 1995, 2001). The lower ionization UV absorbers could also form as condensations out of the hot phase or might be ambient gas swept up by the flow. Alternatively, the low ionization absorbers may have no physical connection to the high-ionization gas and simply lie along the same line-of-sight.

4. Discussion

We have modeled the X-ray absorption in NGC 4151 with 5 independent components, at least three of which are observed at roughly the same radial velocities. The absorbers span a wide range in ionization and are not in close pressure equilibrium. Based on their large covering factors, the more distant absorbers must be screened by those closer to the central source. Furthermore, the evidence for bulk motion (Section 3.4) suggests that there is a large non-radial component to the outflow velocities, as might result if the source gas were rotating around the central black hole (e.g. the accretion disk). Given the physical conditions predicted by our models, we can begin to probe the dynamics of the outflow.

Based on the factor of ~ 3 decrease in the column density of D+Ea, we can estimate its transverse velocity. The size of the broad-line region in NGC 4151 is estimated to be $\approx 8.5 \times 10^{15}$ cm (K. Metzroth et al., in preparation). Since the gas moved out of the line-of-sight over the 26 months between the two HETGS observations, the transverse velocity $v_T \gtrsim 1250$ km s $^{-1}$. If v_T is purely rotational, assuming a black hole mass of $10^{7.1} M_\odot$ (Peterson et al. 2004), D+Ea must have originated at a radial distance $R \lesssim 1.1 \times 10^{17}$ cm from the central potential. Note that this is on the same order as the radial distance estimated from photoionization models of the 1999 STIS spectra (Kraemer et al. 2001), using a density determined from the strength of the C III* lines, a point we address in more detail in Paper II.

Although the outflow is not purely radial, radiation pressure may play a role in accelerating the gas. The least efficient process by which gas can be radiatively accelerated is the scattering of photons off electrons. Other sources of opacity within the gas include line opacity (e.g, Castor et al. 1975), bound-free transitions (Arav, Li, & Begelman 1994; Chelouche & Netzer 2001), and dust (e.g. Konigl & Kartje 1994); the latter is of minimal importance in the absorbing gas in NGC 4151, given the near absence of intrinsic extinction along our line-of-sight to the nucleus (Crenshaw & Kraemer 2005). The ratio of the line and bound-free acceleration to that of electron scattering is the “Force Multiplier” (FM). For $FM = 1$, the source must radiate at its Eddington Luminosity (L_E) to generate an outflow. As such, FM must be $\geq (L_{bol}/L_E)^{-1}$, where L_{bol} is the bolometric luminosity of the AGN, in order to radiatively drive gas from the nucleus. For a typical SED, $L_{bol} \sim 9 \times \lambda L_\lambda(5100\text{\AA})$, where $L_\lambda(5100\text{\AA})$ is the continuum luminosity at 5100 Å (Kaspi et al. 2000b). For $\log \lambda L_\lambda(5100\text{\AA}) \approx 42.88$ (Peterson et al. (2004), NGC 4151 is radiating at $\sim 0.04L_E$, therefore radiative driving can only occur in gas with $FM \geq 25$. Fig 14 shows FM as a function of U for models generated with our assumed SED. These values were computed for the optically thin case, which is the case when radiative acceleration is most effective (the average FM within a cloud decreases as the gas becomes optically thick; see Chelouche & Netzer [2005]). Clearly, X-High is too highly ionized to be radiatively driven in NGC 4151. While the low-ionization components have sufficiently high values of FM , D+Ea is only marginally susceptible to radiative driving. Interestingly, while a substantial fraction, perhaps most, of the gas cannot be radiatively driven, the absorbers seem to possess similar outflow velocities.

Another mechanism for the acceleration of gas is via thermal winds (e.g., Begelman, McKee, & Shields, 1983), arising either from an accretion disk or the putative molecular torus (Krolik & Begelman 1986, 1988) and subsequently accelerated along thermal pressure gradients (Balsara & Krolik 1993; Chelouche & Netzer 2005). One may define an “escape temperature” for the gas, $T_g = GMm_H/R_0k$, where M is the central mass, m_H is the mass of a hydrogen atom, R_0 is the distance to the attracting mass, and k is Boltzmann’s constant

(see Crenshaw et al. 2003, and references therein). If $T > T_g$, a thermal wind will arise. Based on the predicted temperature, one can determine the minimum radial distance at which such an outflow can form, i.e., at a distance $R \geq R_0$. The most likely candidate for a thermal wind is the component X-High. To determine the range of physically plausible radial distances, we impose the constraint that the ratio of the physical depth of the absorber, $\Delta R = N_H/n_H$, to its radial distance, R , be less than unity. From Equation (1), Q (see Section 3.2), and our predicted U for X-High (Table 2), we find that $R \approx 1.6 \times 10^{20} n_H^{-1/2}$ cm. For $\log N_H = 22.5$ and $\Delta R/R \leq 1$, $R \leq 8.3 \times 10^{17}$ cm. Cloudy predicts a temperature for X-High of $T_e = 3.0 \times 10^6$ K. If we assume that any mass other than that of the central black hole is negligible, $R_0 \geq 7.1 \times 10^{18}$ cm. Therefore, X-High cannot have formed as a thermal wind under these conditions. It is possible that the individual X-ray and UV components are borne by a hotter wind, but it must be so highly ionized that it produces no detectable absorption features. Such a wind would lie on the Compton-cooled part of the thermal stability curve, where $T_e \sim 3 \times 10^7$ K, and it would have formed at a radial distance $R \sim 6.7 \times 10^{17}$ cm. However, this places the wind at a larger distance than that estimated for component D+Ea, either by means of the constraints from the bulk motion or from previous photoionization models (Kraemer et al. 2001).

If the absorbers originate within the accretion disk, they may be accelerated via accretion-driven winds (Rees 1987). Models of disk-driven magneto-hydrodynamic (MHD) models predict that gas will flow outwards along (locally) open, rotating magnetic field lines (see Blandford & Payne 1982; Emmering, Blandford, Shlosman, 1992). Bottorff et al. (2000) applied MHD flows to the intrinsic absorption in Seyfert 1 galaxies. Not only do such flows possess large non-radial velocities, but Bottorff et al. predicted that the most highly ionized gas would exist at the smallest radial distances. As noted in Section 3.2, the relationship between ionization state and relative radial distance is suggested by the large covering factors of the individual absorbers. For magnetically confined clouds in the presence of non-dissipative MHD waves, line widths can greatly exceed the thermal widths, particularly if the magnetic field is in equipartition with the gravitational energy density (Bottorff & Ferland 2000, and references therein⁴). This scenario could explain the broad line profiles from component D+Ea and provide a mechanism for pressure confinement if D+Ea is co-located with X-High. Therefore, although we cannot rule out a thermal wind origin and radiative acceleration may be important for the lower ionization components, we suggest that the absorption in NGC 4151 is most consistent with an MHD flow.

Independent of the mechanism driving the outflow, we can use the model parameters to

⁴Although Bottorff & Ferland treat the case of broad emission lines, the same analysis applies to absorption lines.

constrain the mass outflow rate. For a spherical outflow, the mass of the absorber is given by $M_{abs} = 4\pi r^2 N_H m_p C_g$, where m_p is the proton mass and C_g is the global covering factor. C_g can be constrained by comparing the predicted emission-line fluxes to the observed line luminosities. The model for D+Ea predicts a flux = $5.7 \times 10^5 \text{ erg s}^{-1} \text{ cm}^{-2}$ for the O VII λ 22.1 line (the forbidden line of the He-like triplet). The measured flux is $\approx 3.5 \times 10^{-13} \text{ erg s}^{-1} \text{ cm}^{-2}$, which yields a luminosity $\sim 7.3 \times 10^{39} \text{ ergs s}^{-1}$. For a radial distance of $r = 10^{17} \text{ cm}$, $C_g \sim 0.1$, which is an upper limit since much of the O VII emission is extended (as we will discuss in Paper III). Thus, $M_{abs} \lesssim 0.3M_\odot$. Note that this is the mass of D+Ea alone; there could be a similar amount of mass from X-High. The average mass loss rate is $\dot{M}_{abs} = M_{abs}/t_c$, where $t_c = r/v_r$ is the radial travel time. If the flow originates at the origin ($r = 0$), we obtain $\dot{M}_{abs} \sim 0.005M_\odot \text{ yr}^{-1}$ and a kinetic luminosity $1/2\dot{M}_{abs}v_r^2 \sim 4 \times 10^{38} \text{ ergs s}^{-1}$. Assuming an efficiency of 0.1 (see Peterson 1997), L_{bol} requires a mass accretion rate of $\dot{M} \sim 0.001M_\odot \text{ yr}^{-1}$ and, thus, based on this set of assumptions, the outflow and accretion rates are comparable, similar to the case in NGC 3516 (Crenshaw et al. 2003). However, if the flow originates far from the continuum source, \dot{M}_{abs} could be much greater, which would require the flow to be continuously replenished (Netzer et al. 2003; Chelouche & Netzer 2005).

5. Summary

We have used the *Chandra*/HETGS and photoionization models to probe the physical conditions in the X-ray absorbing gas in the Seyfert 1 galaxy NGC 4151. Our models are further constrained by covering factors, radial velocities, and ionic column densities derived from simultaneous UV spectra obtained with *HST*/STIS and *FUSE*. We compared the 2002 HETG spectrum with one obtained during 2000 when NGC 4151 was in a lower flux state. The soft X-ray emission in both epochs is dominated by emission lines, which have not varied in flux. Hence there is a negligible contribution from the transmitted continuum below 1 keV.

We find evidence for at least two distinct X-ray absorbers: high-ionization gas (X-High), in which absorption lines from H-like Mg, Si, and S arise, and a less ionized component, in which inner shell absorption lines from these elements form. We identify the latter with the UV absorption at -491 km s^{-1} , component D+E in Kraemer et al. (2001). Interestingly, X-High has a similar radial velocity. We have also included three additional absorbers in our models: a high density component, D+Eb, a lower covering factor component, D+Ec, both associated with the UV component at -491 km s^{-1} , and UV component E'. Since all the components other than D+Ec cover $> 80\%$ of the continuum source, they must screen each

other from the ionizing radiation. Based on their relative opacities, we suggest that X-High is closer to the central source than D+E a , followed by the additional UV components. Our model predicts both broad-band features and absorption lines in good agreement with the 2002 HETG spectrum. The absorbers are not in pressure equilibrium with each other, which suggests (as does our screening scenario) that the individual components are not co-located, although we cannot rule this out if magnetic confinement is important (e.g. Gabel et al. 2005). While the models predict that each of the X-ray absorbers is thermally stable, X-High may become unstable if the continuum flux in NGC 4151 drops sufficiently. Hence, it is possible that lower ionization gas could have formed from the high ionization component of the flow during previous low flux states.

The parameters for X-High ($\log U = 1.05$, $\log N_H = 22.5$) are similar to those of the high ionization absorbers detected in *Chandra* and *XMM-Newton* spectra of NGC 3783 (Netzer et al. 2003; Behar et al. 2003) and NGC 3516 (Turner et al. 2005), although the latter possesses an additional component with a much higher column density but small covering factor. We find that X-High is too highly ionized to be radiatively accelerated in a source as sub-Eddington as NGC 4151. The presence of similar high-ionization, high-velocity gas in these three well-studied Seyferts is an indication that this hitherto undetected component may hold the key to the dynamics of mass outflow.

We also analyzed the 2000 HETG spectrum, when the intrinsic continuum flux was ~ 2.5 times weaker. We find that the heavier X-ray absorption reveals the combined effects of the lower ionization state of the intervening gas and a higher column density of component D+E a . This requires $v_T \gtrsim 1250$ km s $^{-1}$. If this is a rotational component, it places the absorber at a radial distance of $\lesssim 1.1 \times 10^{17}$ cm. Given the predicted T_e , if X-High is co-located with D+E a , it cannot be thermally expanding away (i.e., from the disk). Furthermore, our model constrains X-High to lie well within the point where its predicted temperature equals its escape temperature. Therefore, the most plausible acceleration mechanism for the gas is a disk-driven MHD flow.

Although we have been able to probe more deeply than ever into the nature of the intrinsic absorption in NGC 4151, there are still a number of open issues. Unless the components are co-located, we do not know why the outflow velocities for X-High and the various components of D+E are similar. Determining how the absorbers are radially driven requires detailed modeling, in particular with MHD codes, that is beyond the scope of this paper. Finally, although we have determined that the gas must have a large transverse velocity, we cannot determine whether this is in the plane of the disk (i.e., due to rotation) or perpendicular to it.

S.B.K., I.M.G., and J.R.G. acknowledge support from Smithsonian grant GO2-3138A. H.N. acknowledges support by the Israel Science Foundation grant 232/03. E.B. was supported by grant No. 2002111 from the United States Israel Binational Foundation. We thank Gary Ferland for providing us an updated version of Cloudy.

REFERENCES

- Arav, N., Li, Z.-Y., & Begelman, M.C. 1994, *ApJ*, 432, 62
- Barr, P., White, N.E., Sanford, P.W., & Ives, J.C. 1977, *MNRAS*, 181, 43P
- Behar, E., & Netzer, H., 2002, *ApJ*, 570, 165
- Behar, E., Rasmussen, A.P., Blustin, A.J., Sako, M., Kahn, S.M., Kaastra, J.S., Branduardi-Raymont, G., & Steenbrugge, K.C. 2003, *ApJ*, 598, 232
- Begelman, M.C., McKee, C.F., & Shields, G.A., 1983, *ApJ*, 271, 70
- Blandford, R.D., & Payne, D.G., 1982, *MNRAS*, 199, 883
- Boksenberg, A., et al. 1978, *Nature*, 275, 404
- Bottorff, M.C., & Ferland, G.J. 2000, *MNRAS*, 316, 103
- Bottorff, M.C., Korista, K.T., & Shlosman, I. 2000, *ApJ*, 537, 134
- Brinkman, A.C., Gunsing, C.J., Kaastra, J.S., Braeuninger, H.W., Hartner, G.D., Predehl, P., Drake, J.J., Juda, J.Z., Juda, M., Dewey, D., Flanagan, K.A., & Marshall, H.L. 1997, *Proc. SPIE*, 3113, 181
- Bromage, G.E., et al. 1985, *MNRAS*, 251, 1
- Chelouche, D., & Netzer, H., 2001, *MNRAS*, 326, 916
- Crenshaw, D.M., & Kraemer, S.B. 1999, *ApJ*, 521, 572
- Crenshaw, D.M., & Kraemer, S.B. 2005, *ApJ*, 625, 680
- Crenshaw, D.M., Kraemer, S.B., Boggess, A., Maran, S. P., Mushotzky, R.F., & Wu, C.-C. 1999, *ApJ*, 516, 750
- Crenshaw, D.M., Kraemer, S.B., & George, I.M. 2003, *ARA&A*, 41, 117
- Crenshaw, D.M., Kraemer, S.B., Hutchings, J.B., Danks, A.C., Gull, T.R., Kaiser, M.E., Nelson, C.H., & Weistrop, D. 2000, *ApJ*, 545, L27
- Crenshaw, D.M., et al. 1996, *ApJ*, 470, 322
- de Vaucouleurs, G., de Vaucouleurs, A., Corwin, H.G., Jr., Buta, R.J., Paturel, G., & Fouque, P. 1991, *Third Reference Catalogue of Bright Galaxies* (New York: Springer)
- Edelson, R.A., et al. 1996, *ApJ*, 470, 364
- Emmering, R.T., Blandford, R.D., & Shlosman, I., 1992, *ApJ*, 385, 460
- Gabel, G.R. et al., 2005, *ApJ*, submitted

- Garmire, G.P., Bautz, M.W., Ford, P.G., Nousek, J.A., & Ricker, G.R., 2003, in *X-Ray and Gamma-Ray Telescopes and Instruments for Astronomy*, eds. J.E.Trümper, H.D. Tananbaum, Proc. SPIE 4851, 28
- George, I.M., & Fabian, A.C., 1991, MNRAS, 249, 352
- George, I.M., Turner, T.J., Netzer, H., Nandra, K., Mushotzky, R.F., & Yaqoob, T. 1998, ApJS, 114, 73
- Grevesse, N., & Anders, E. 1989, in *Cosmic Abundances of Matter*, ed. C.J. Waddington (New York: AIP), 1
- Gu, M. 2003, ApJ, 590. 1131
- Hamann, F., Barlow, T.A, Junkkarinen, V., & Burbidge, E.M. 1997, ApJ, 478, 80
- Ives, J.C., Sanford, P.W., & Penston, M.V. 1976, ApJ, 207, L159
- Kaastra, J.S., Mewe, R., Liedahl, D.A., Komossa, S., & Brinkman, A.C. 2000, A&A, 354, L83
- Kaastra, J.S., et al. 2002, A&A, 386, 427
- Kaspi, S., Smith, R.S., Netzer, H., Maoz, D., Janunuzi, B.T., & Giveon, U. 2000b, ApJ, 533, 631
- Kaspi, S., et al. 2000a, ApJ, 535, L17
- Kaspi, S., et al. 2001, ApJ, 554, 216
- Kaspi, S., et al. 2002, ApJ, 574, 643
- Königl, A., & Kartje, J. 1994, ApJ, 424, 446
- Kraemer, S.B., Crenshaw, D.M., George, I.M., Netzer, H., Turner, T.J., & Gabel, J.R. 2002, ApJ, 577, 98
- Kraemer, S.B., Crenshaw, D.M., Hutchings, J.B., George, I.M., Danks, A.C., Gull, T.R., Kaiser, M.E., Nelson, C.H., Weistrop, D., & Vieira, G.L. 2001, ApJ, 551, 671
- Kraemer, S.B., Ferland, G.J., & Gabel, J.R. 2004, ApJ, 604, 556
- Kriss, G.A. 2002, in *Mass Outflow in Active Galactic Nuclei: New Perspectives*, ed. D.M. Crenshaw, S.B. Kraemer, and I.M. George, ASP Conf. Ser. 255, 69
- Kriss, G.A., Davidsen, A.F., Zheng, W., Kruk, J.W., & Espey, B.R. 1995, ApJ, 454, L7
- Kriss, G.A., et al. 1996, ApJ, 467, 629
- Kriss, G.A., et al. 1992, ApJ, 392, 485
- Krolik, J.H, & Begelman, M.C. 1986, ApJ, 308, L55

- Krolik, J.H., & Begelman, M.C. 1988, ApJ, 329, 702
- Krolik, J.H., & Kriss, G.A. 1995, ApJ, 447, 512
- Krolik, J.H., & Kriss, G.A. 2001, ApJ, 561, 684
- Krolik, J.H., McKee, C.F., & Tarter, C.B. 1981, ApJ, 249, 422
- Marshall, H.L., Dewey, D., & Ishibashi, K. 2004, in *X-Ray and Gamma-Ray Instrumentation for Astronomy XIII*, eds K.A. Flanagan, O.H.W. Siedmund, Proc. SPIE 5165, 457
- Marshall, H.L., Tennant, A., Grant, C.E., Hitchcock, A.P., O'Dell, S.L., & Plucinsky, P.P. 2004, in *X-Ray and Gamma-Ray Instrumentation for Astronomy XIII*, eds K.A. Flanagan, O.H.W. Siedmund, Proc. SPIE 5165, 497
- Mathur, S., Wilkes, B.J., Elvis, M., & Fiore, F. 1994, ApJ, 434, 493
- Matt, G., Perola, G.C., & Piro, L. 1991, A&A, 247, 25
- Matt, G., Fabian, A.C., & Reynolds, C.S. 1997, MNRAS, 289, 175
- Murphy, E.M., Lockman, F.J., Laor, A., & Elvis, M. 1996, ApJS, 105, 369
- Murray, N., Chiang, J., Grossman, S.A., & Voit, G.M. 1995, ApJ, 451, 498
- Netzer, H., et al. 2003, ApJ, 599, 933
- Ogle, P.M., Marshall, H.L., Lee, J.C., Canizares, C.R. 2000, ApJ, 545, L81
- Peterson, B.M. 1997. *An Introduction to Active Galactic Nuclei*. Cambridge, UK: Cambridge Univ. Press .
- Peterson, B.M., et al. 2004, ApJ, 613, 682
- Rees, M.J. 1987, MNRAS, 228, P47
- Reynolds, C.S. 1997, MNRAS, 286, 513
- Schurch, N.J., & Warwick, R.S. 2002, MNRAS, 334, 811
- Turner, T.J., Kraemer, S.B., George, I.M., Reeves, J.N., & Bottorff, M.C. 2005, ApJ, 618, 155
- Verner, D.A., Ferland, G.A., Korista, K.T., & Yakovlev, D. G. 1996, ApJ, 465, 487
- Weaver, K.A., Yaqoob, T., Holt, S.S., Mushotzky, R.F., Matsuoka, M., & Yamauchi, M. 1994, ApJ, 436, L27
- Weymann, R.J., Morris, S.L., Gray, M.E., & Hutchings, J.B. 1997, ApJ, 483, 717
- Yaqoob, T., Warwick, R.S. 1991, MNRAS, 248, 773
- Yaqoob, T., Warwick, R.S., & Pounds, K.A. 1989, MNRAS, 236, 153

Zdziarski, A.A., Johnson, W.N., & Magdziarz, P. 1996, MNRAS, 283, 193

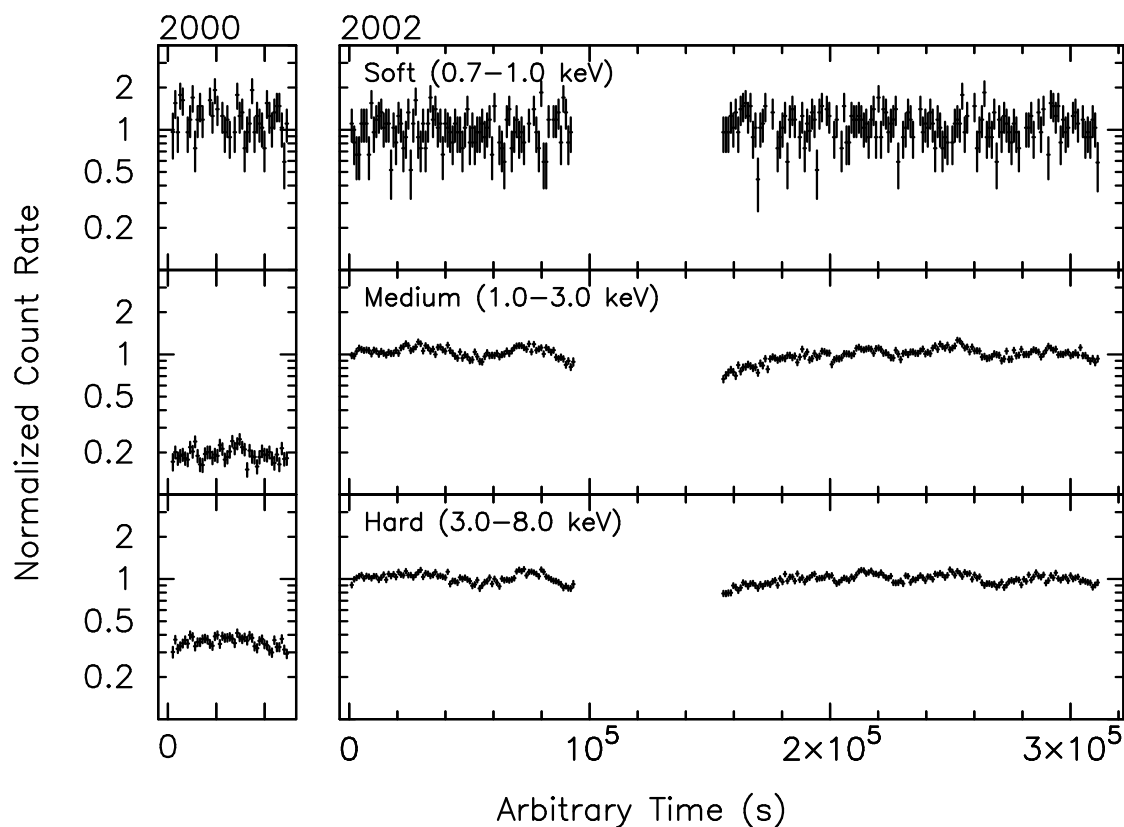


Fig. 1.— Coadded MEG and HEG 1st-order light curves, using 1024s bins, from the two HETGS observations discussed here. For simplicity the light curves in each band have been renormalized to the mean count rate obtained during the 2002 observations. In the soft (0.5–1.0 keV) band, the light curves are consistent with a single constant flux both within each observation, and at each epoch. Variability is apparent during both observations in the medium (1.0–3.0 keV) and hard (3.0–8.0 keV) bands. More dramatically, NGC 4151 brightened considerably in these bands between 2000 and 2002, with the larger fractional increase occurring in the medium band.

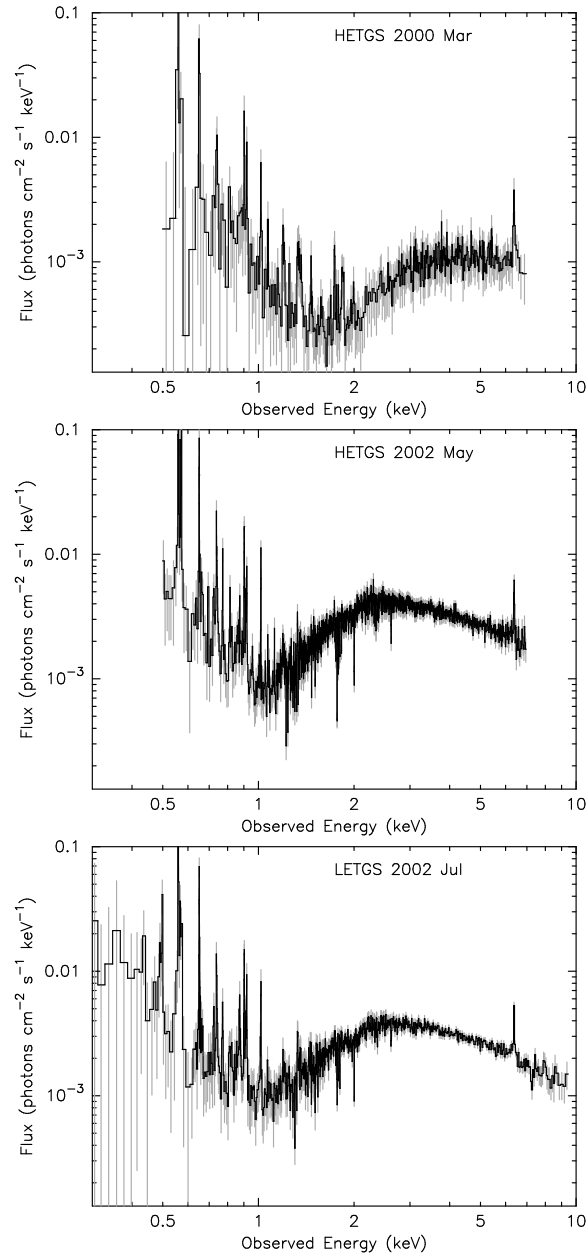


Fig. 2.— Time-averaged, broad-band spectra for each of the *Chandra* observations of NGC 4151 discussed here (MEG data only for the HETGS observations). In each case, the data have been corrected for the appropriate instrumental response, and (for clarity) rebinned such that each bin contains at least 30 photons. (Note this process clearly smooths out a number of the sharp emission and absorption features discussed later in the text). Error bars are shown in gray. The low energies the spectra are dominated by emission lines, and are almost identical at all epochs. However above 1 keV, the emission is dominated by the nuclear continuum. This is very similar in both form and intensity for the two observations in 2002, but stronger and of a different shape to that observed in 2000.

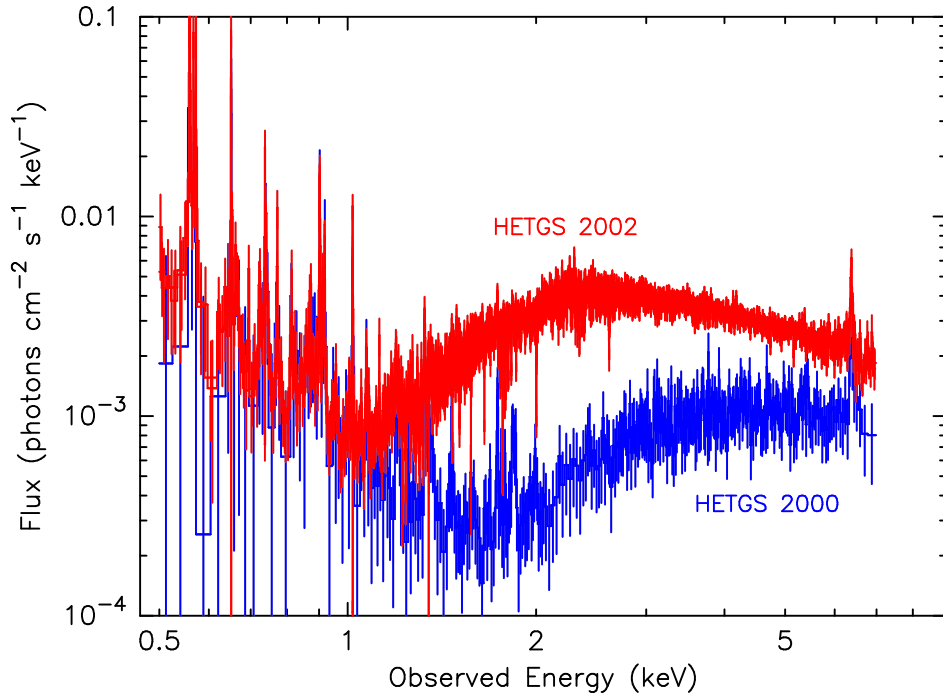


Fig. 3.— A comparison of the 2000 (blue) and 2002 (red) HETGS data of NGC 4151. As in Fig.2, the data have been rebinned such that each bin contains at least 30 photons. During both epochs, the flux at energies < 1 keV is dominated by unocculted line emission, which does not appear to have varied in flux.

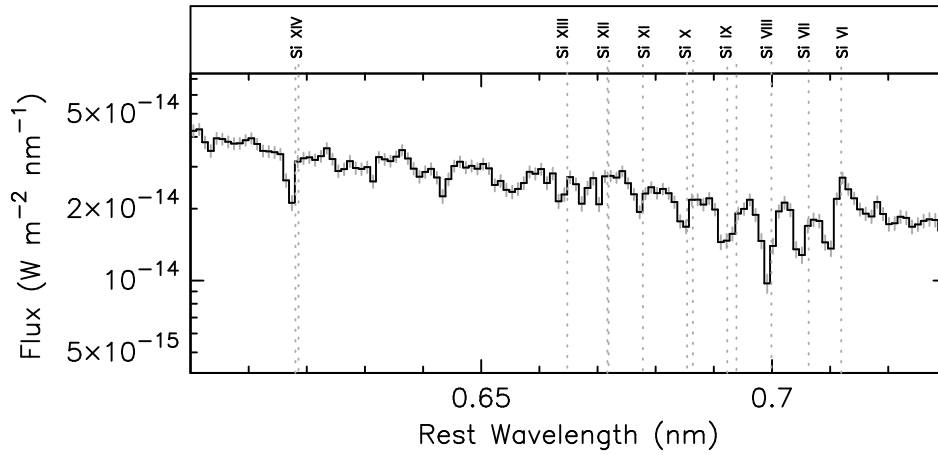


Fig. 4.— A section of the combined MEG/HEG spectrum showing the lines from Si VI to Si XIV using a binsize of 0.01\AA . The Si XIV appears deeper than Si XIII and the lower ionization states appear to peak near Si VIII, which strongly suggests that there are at least two absorbers with differing ionization states. Also, note that the lines appear systematically blue-shifted, similar to the UV lines, which suggests mass outflow.

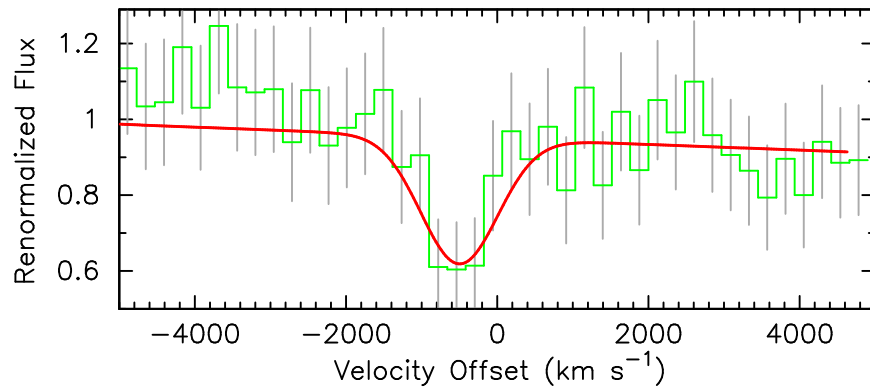


Fig. 5.— The Si XIV line profile from the 2002 HETGS spectrum is shown as a function of velocity. The binsize is 0.005 \AA , which is 1σ for the HEG resolution, however both MEG and HEG are combined, so model is smoothed by MEG resolution. The uncertainties are shown via the grey lines. We have overlaid a Gaussian profile as a guide to demonstrate the velocity offset (v_r) with respect to systemic. We determine v_r to be $\sim -500 \text{ km s}^{-1}$.

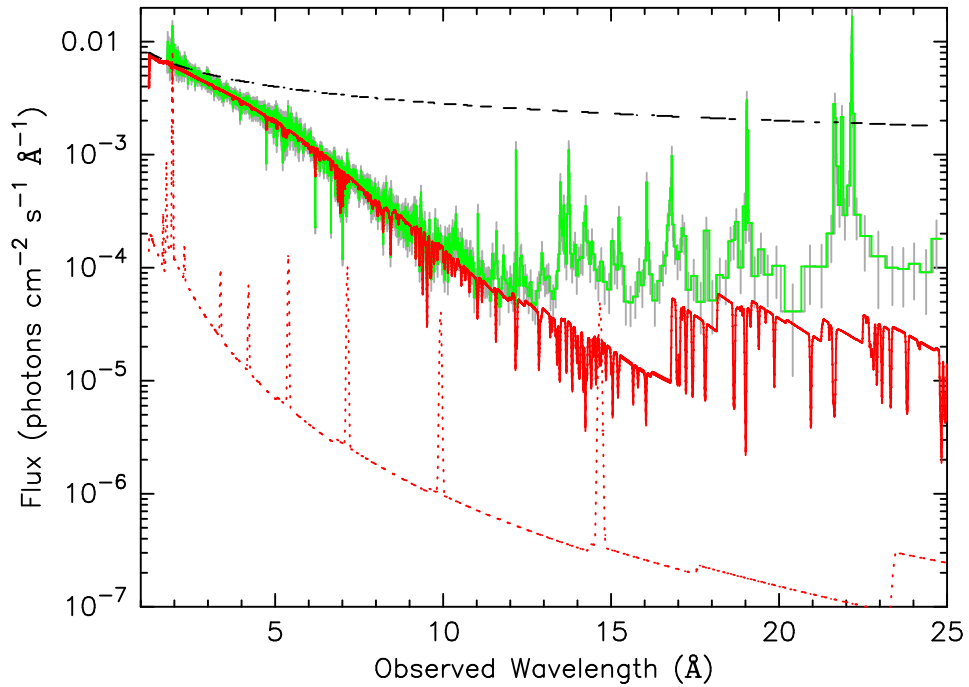


Fig. 6.— The model absorbed continuum (red), including the reflection component (dotted red line), is shown versus the 2002 HETGS data (green). At wavelengths shorter than ~ 12 Å (~ 1 keV), the model reproduces the curvature in the observed continuum, while at longer wavelengths the absorber/transmitted continuum lies below the observed points, indicating that the soft flux is dominated by unocculted emission.

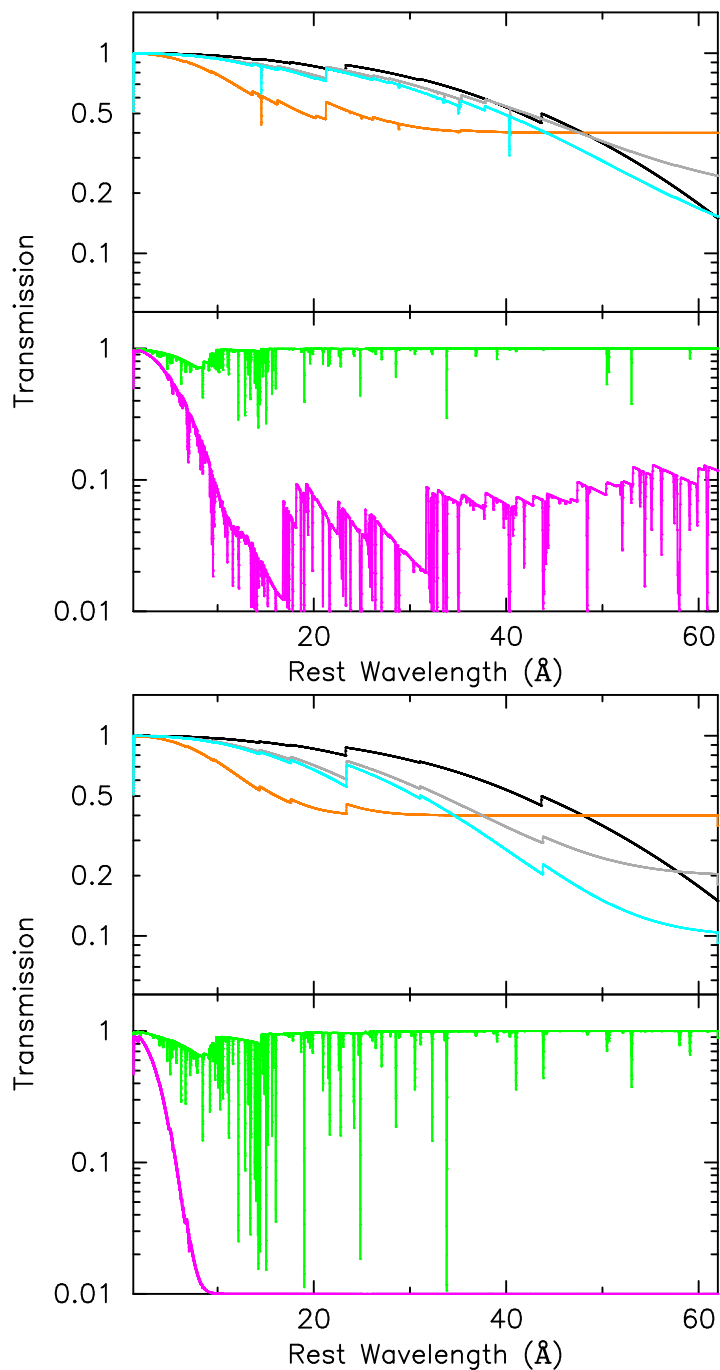


Fig. 7.— The upper panel shows the broad-band transmission curves for each of the model components for the 2002 epoch discussed in the text. The lower panel shows the predicted curves for the 2000 intensity state. In all cases E' is grey, $D+Ec$ is orange, $D+Eb$ is blue, $D+Ea$ is magenta, and X-High is green. The Galactic component is shown in black. Note that components E' , $D+Ec$ and $D+Eb$ only partially cover the source, resulting in their curves flattening towards longer wavelengths due to the unocculted fraction.

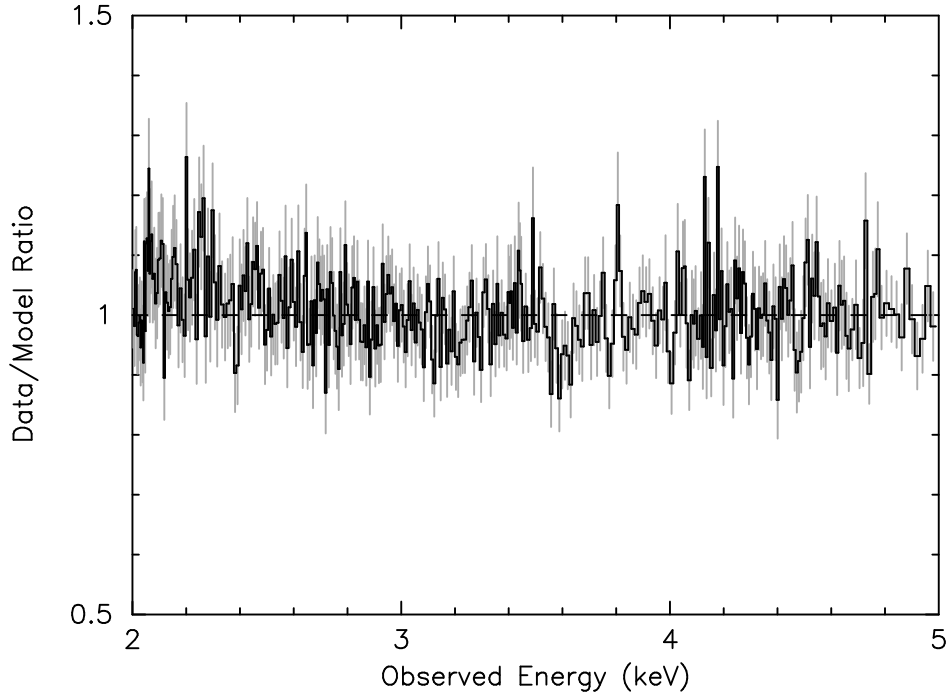


Fig. 8.— The $\pm 1^{\text{st}}$ -order MEG (only) data divided by the model for the 2002 obs. The data are plotted such that each bin contained at least 200 photons for clarity. A few unmodeled features are present, and there is an indication of a small systematic excess of the data compared to the data towards the lowest energies. However the effect is at a level of $\lesssim 10\%$, and hence at a similar level and sense as the current uncertainties in the calibration associated with the Ir coating on Chandra’s mirrors. Furthermore, NGC 4151 does exhibit some variability during the observation, yet here we restrict our analysis to the time-averaged spectrum. With these facts in mind, we consider our model to provide an adequate match to the overall spectral curvature in the time-averaged spectrum.

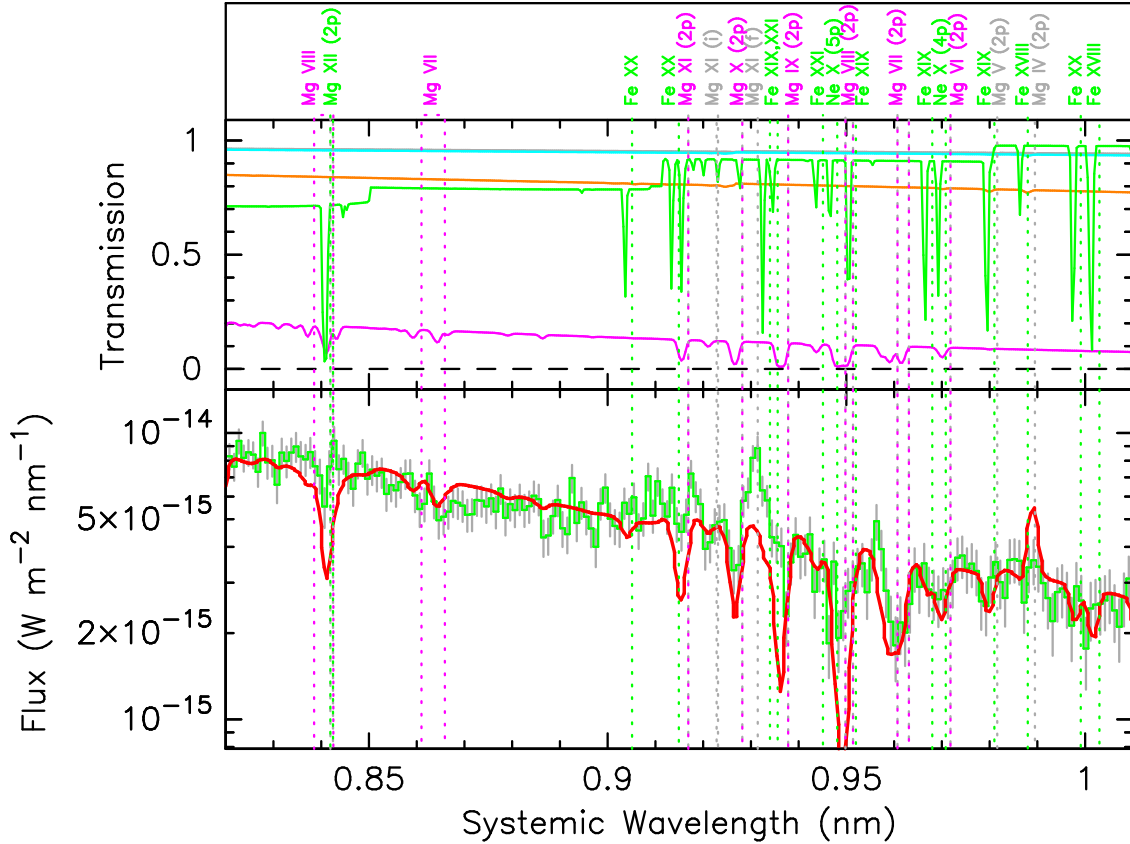


Fig. 9.— The region of the time-averaged spectrum obtained from the 2002 HETGS observation of NGC 4151 showing the Mg lines. The lower panels shows (in green) the coadded MEG and HEG 1st-order spectra (after instrumental corrections have been applied, and assuming a systemic $z = 0.003319$) using 0.01 Å bins. We note that absorption lines due to transitions to the 3p level are also evident in the data for Mg VII. The model spectrum discussed in the text is shown by the red curve (after smoothing by the instrumental resolution). The upper panels show the intrinsic transmission curves of the individual components to the model. As in Fig. 7, D+Ec is orange, D+Eb is blue, D+Ea is magenta, and X-High is green. Also shown are the locations of several absorption lines (color-coded for the component dominating the feature).

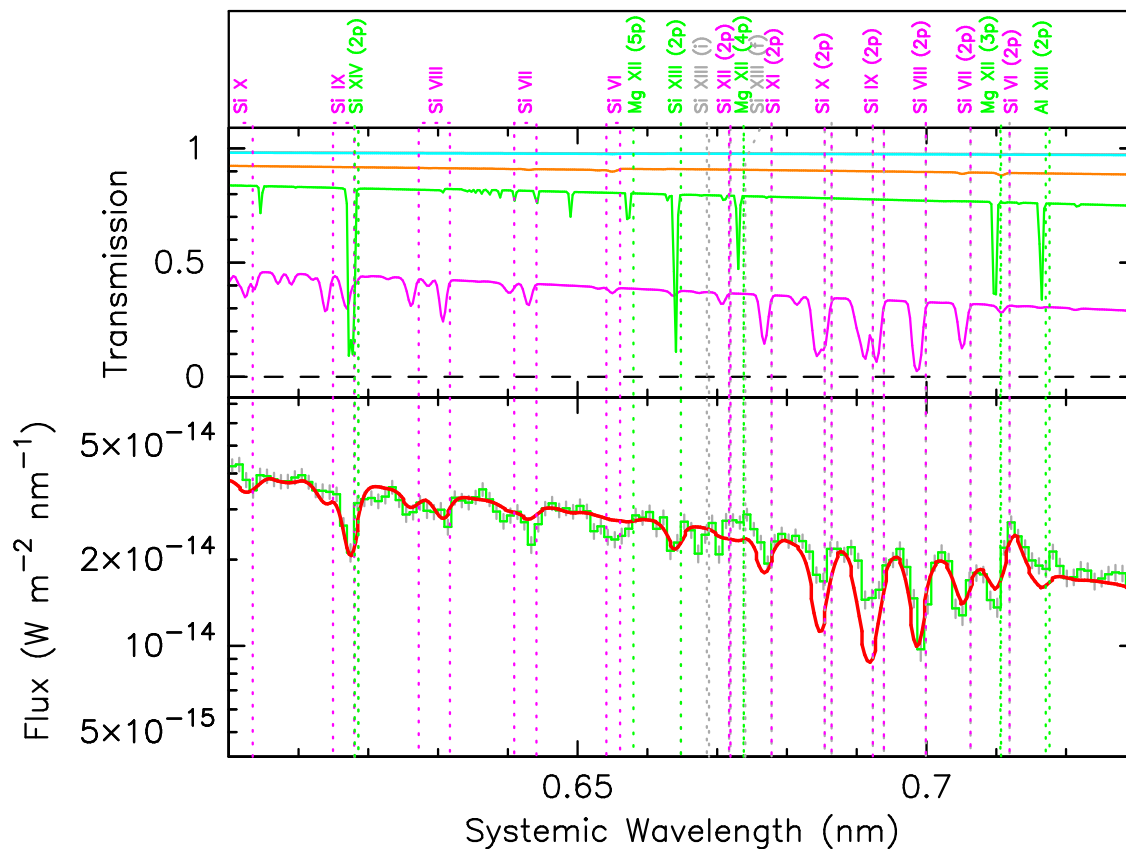


Fig. 10.— The regions of the time-averaged spectrum obtained from the 2002 HETGS observation of NGC 4151 showing the Si lines. Color-code and model parameters are the same as described for Fig 9. Absorption lines due to transitions to the $3p$ level are also evident in the data for Si VII and Si VIII.

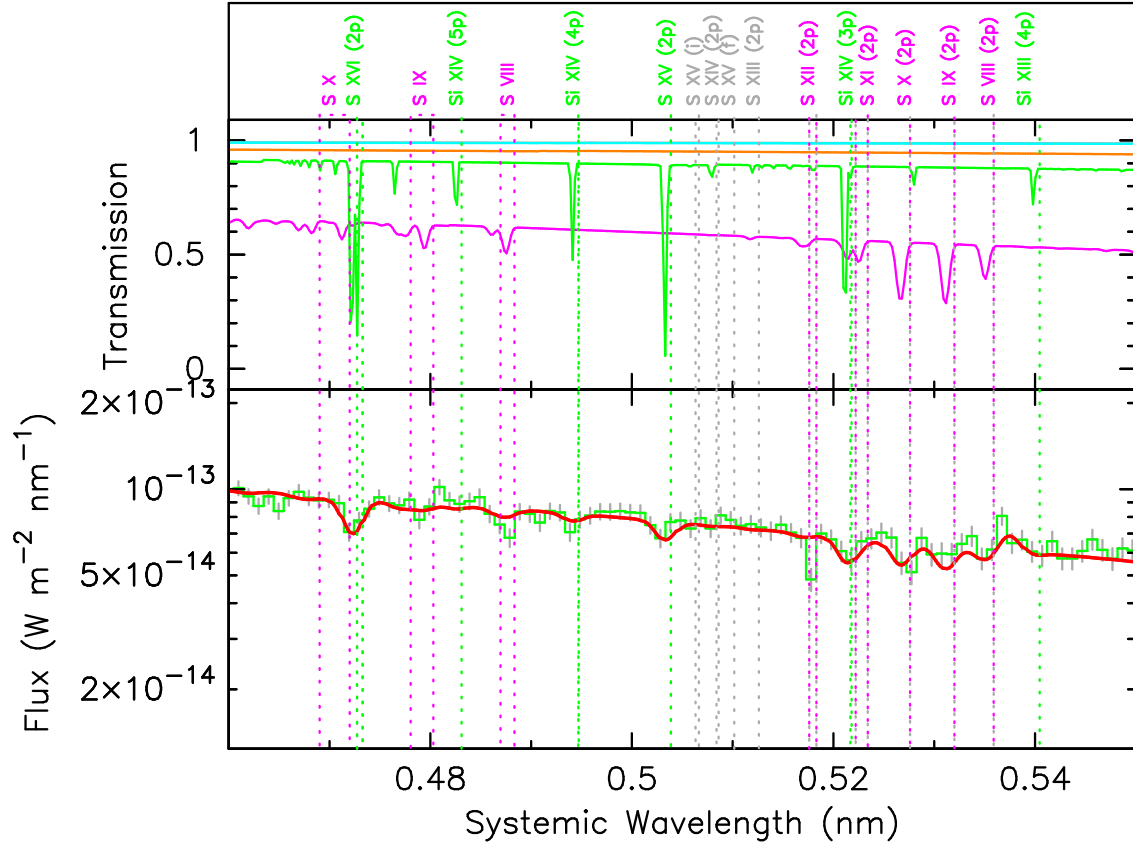


Fig. 11.— The regions of the time-averaged spectrum obtained from the 2002 HETGS observation of NGC 4151 showing the S lines. Color-code and model parameters are the same as described for Fig 9. Absorption lines due to transitions to the $3p$ level are also evident in the data for S VIII and S IX.

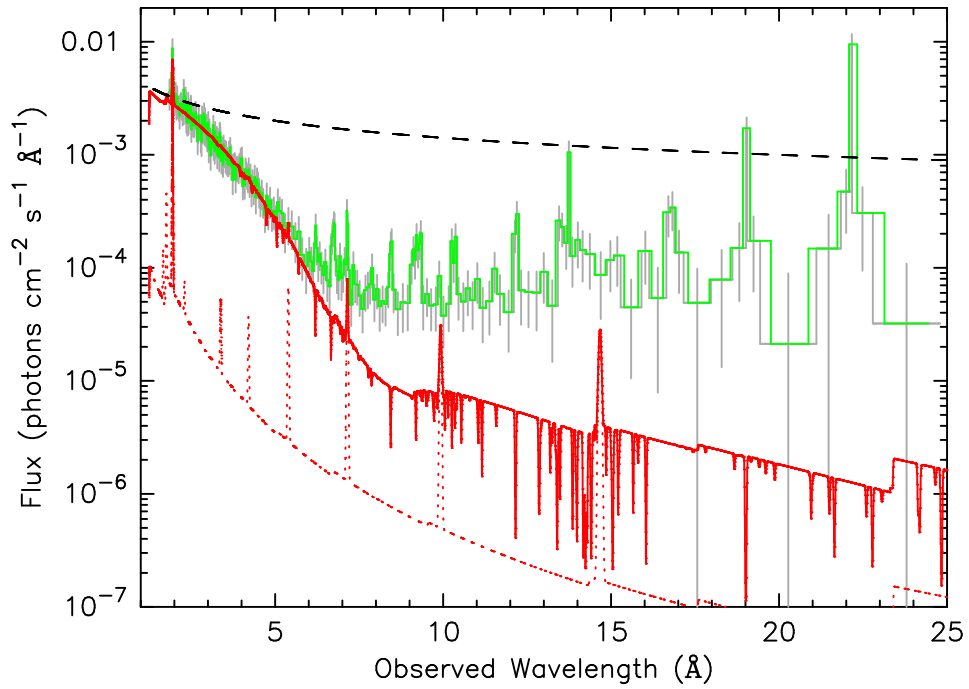


Fig. 12.— The model absorbed continuum (red), including the reflection component (dotted red line), is shown versus the 2000 HETGS data. For the model the ionizing flux was decreased by a factor of 2 and the column density of component D+Ea was increased by a factor of 3 compared to the 2002 model.

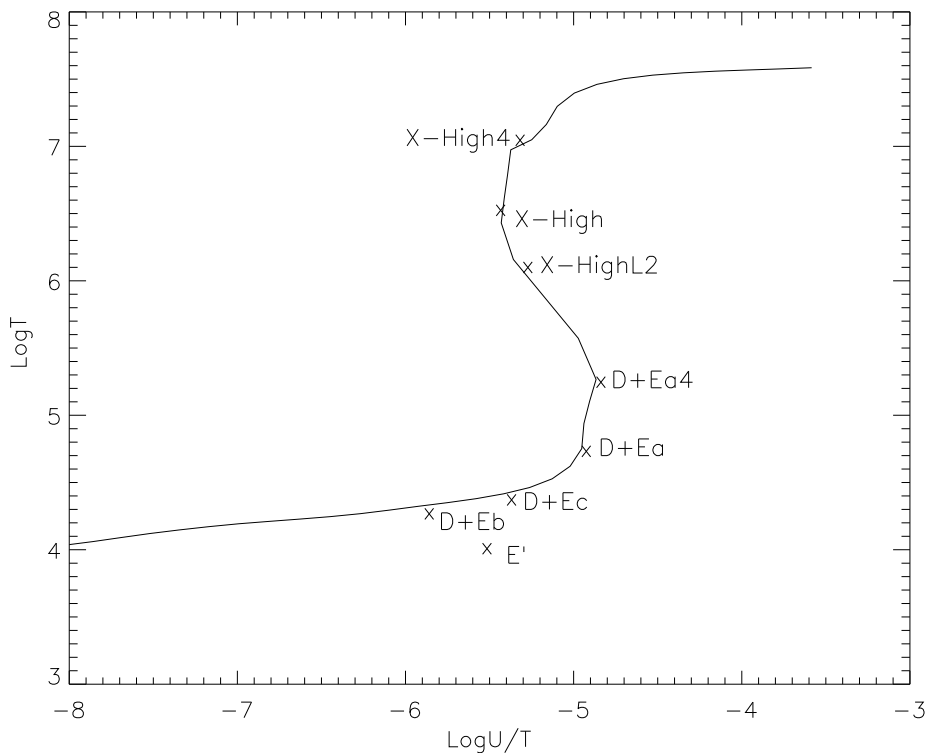


Fig. 13.— Thermal Stability curve for optically-thin models generated with the same SED used for the absorbers. The positively sloped sections, at low and high temperatures, are the line-cooled and Compton -cooled regions, respectively. As noted in the text, the vertical regions are quasi-stable, while the region with negative slope is unstable to thermal perturbations. The values for each absorber component are shown (see text), as well as those for a source luminosity 4 times greater than during the 2002 observations (D+Ea4 and X-High4) and 2 times weaker, as during the 2000 HETGS observations (X-HighL2).

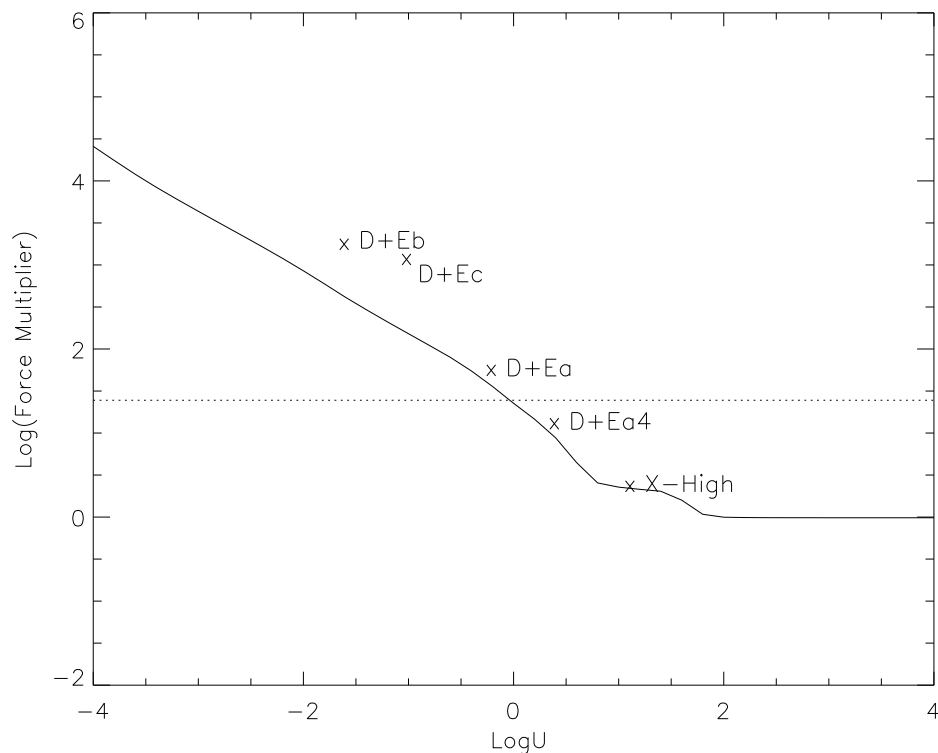


Fig. 14.— The predicted Force Multipliers (FM) are shown as a function of U for optically thin models assuming the same SED used for the absorbers. The horizontal line shows the minimum value of FM required to accelerate the gas for a source radiating at $0.04L_E$ (see text). The values for X-High and each component of D+E are shown, as well as the locations for for a source luminosity 4 times greater than during the 2002 observations (D+Ea4). The screened models lie off the curve since the fractional ionization as a function of U is lower due to the paucity of photons at the He II Lyman limit..

Table 1. Model Constraints from UV spectra

Component	C_f^a	v_r^b	σ_v^c	$\log(N/\text{cm}^{-2})^d$	Model Prediction
D+Ea	0.9	-491(± 8)	185	$\log N_{OVI}: > 15.0$ $\log N_{NV}: > 15.0$ $\log N_{CIV}: > 15.0$	see Table 3
D+Eb	0.8	-491(± 8)	185	C III*: $\log N_{j=0} < 14.5$ $\log N_{j=1} < 14.3$ $\log N_{j=2} \geq 14.8$ $\log N_{PV} \lesssim 14.0$	14.1 ^e 14.3 ^e 14.8 ^e 13.4
D+Ec	0.5	-491(± 8)	185	$\log N_{PV} \sim 14.5$	14.5
E'	0.8	-215(± 11)	26	$\log N_{SIV} \gtrsim 15.0$ $\log N_{PV} \sim 13.0$	15.7 13.4

^aThe UV Covering Factor is that of the combined continuum and broad line emission (see Gabel et al. 2005).

^bRadial velocity (km s^{-1} ; Kraemer et al. [2001]).

^cVelocity dispersion (km s^{-1}).

^dIonic column densities are indicated as N_{ion} , where *ion* is the name of the ion.

^eModel results for $\log(n_H) = 8.9$.

Table 2. Final Model Parameters

Component	$\log U^a$	$\log N_H^b$	C_f
X-High	1.05	22.5	1.0
D+E <i>a</i>	−0.27	22.46	1.0
D+E <i>b</i>	−1.67	20.8	0.9
D+E <i>c</i>	−1.08	21.6	0.6
E′	−1.59	20.8	0.8
X-High-2000 ^c	0.75	22.5	1.0
D+E <i>a</i> -2000	−0.57	22.93	1.0

^aThe ionization parameters for the screened components include the effects of absorption by intervening gas.

^b N_H is the total hydrogen column density (in units of cm^{-2}), i.e., $N_H = N_{HI} + N_{HII}$.

^cX-High-2000 and D+E*a*-2000 were generated to fit the 2000 HETGS data. Note that the other components of the 2000 model were not included since they are essentially neutral.

Table 3. Predicted Column Densities^a

Ion	X-High	D+E _a	D+E _b	D+E _c	E'
H I	14.0	17.0	17.1	17.4	17.3
He II	15.4	19.1	19.8	16.4	19.8
C IV		17.2	17.1	18.0	17.1
N V		17.1	14.8	15.8	14.6
O VI		18.5	14.1	15.8	
O VII		19.1			
O VIII	17.6	18.3			
Ne VIII		17.8			
Ne IX	15.7	17.8			
Ne X	17.4	16.7			
Mg V		15.6			
Mg VI		16.7			
Mg VII		17.3			
Mg VIII		17.5			
Mg IX		17.4			
Mg X		16.9			
Mg XI	16.0	16.3			
Mg XII	17.3	15.4			

Table 3—Continued

Ion	X-High	D+E a	D+E b	D+E c	E'
Si VI		16.5			
Si VII		17.2			
Si VIII		17.5			
Si IX		17.4			
Si X		17.1			
Si XI		16.5			
Si XII		15.8			
Si XIII	16.6	15.4			
Si XIV	17.5				
S VII		16.8			
S VIII		17.1			
S IX		17.1			
S X		16.9			
S XI		16.5			
S XII		15.9			
S XIII		15.0			
S XIV	15.3				
S XV	16.8				
S XVI	17.3				

Table 3—Continued

Ion	X-High	D+E a	D+Eb	D+Ec	E'
Fe VII		15.5			
Fe VIII		16.7			
Fe IX		17.5			
Fe X		17.5			
Fe XI		17.4			
Fe XII		17.1			
Fe XIII		16.6			
Fe XIV		16.1			
Fe XV	15.7	15.5			
Fe XVI	16.0				
Fe XVII	17.3				
Fe XVIII	17.7				
Fe XIX	17.6				
Fe XX	17.0				
Fe XXI	16.0				
Fe XXII	15.0				

^aValues are the log of the column densities in units of cm^{-2} . No value is listed if the predicted $N_{ion} < 14.0$ or < 15.0 for those ions constrained by UV or X-ray absorption lines, respectively. Iron and neon are included for completeness.